Distributed Sand-Grain Roughness Effects on Blunt Body Hypersonic Transition and Heating

Brian R. Hollis*
NASA Langley Research Center, Hampton, VA 23681

An experimental investigation of distributed sand-grain surface roughness effects on boundary-layer transition and convective heating has been performed. Two representative entry vehicle geometries, a spherical-cap aeroshell and a sphere-cone aeroshell, were considered. Multiple cast ceramic wind tunnel models of each geometry were fabricated with various roughness heights to simulate an ablated thermal protection system. Wind tunnel testing was performed at Mach 6 over a range of Reynolds numbers sufficient to produce laminar, transitional, and turbulent flow. Aeroheating and boundary-layer transition onset data were obtained using global phosphor thermography. The experimental heating data are presented herein, as are comparisons to laminar and turbulent smooth-wall heat transfer distributions from computational flow field simulations.

I. Nomenclature

D_{ASTM}	ASTM mesh particle diameter specification (m) or (in)
H_0	total enthalpy (J/kg)
H_{AW}	adiabatic wall enthalpy (J/kg)
H_e	boundary layer edge enthalpy (J/kg)
H_k	roughness height enthalpy (J/kg)
H_w	wall enthalpy (J/kg)
h	heat-transfer film coefficient (kg/m^2-s**)**
h_{FR}	Fay-Riddell theory heat-transfer film coefficient
h_{nom}	nominal ASTM mesh particle roughness height (m) or (in)
h_{mean}	mean value of measured roughness heights (m) or (in)
h_{PV}	measured peak-to-valley roughness height (m) or (in)
h_{PV50}	*50*% exceedance value of measured peak-to-valley roughness heights (m) or (in)
h_{RMS}	root-mean-square value of measured roughness heights (m) or (in)
k_{PV}	actual peak-to-valley roughness height (m) or (in)
k_{PV50}	*50*% exceedance value of actual peak-to-valley roughness heights (m) or (in)
M_e	boundary layer edge Mach number
M_∞	free stream Mach number
p_{trans}	geometric transfer parameter for roughness height
r_{stag}	radius of stagnation region M_e boundary (m)
R	model base radius (m)
R_C	model corner radius (m)
R_N	model nose radius (m)
Re_{k+}	roughness height Reynolds number
Re_θ	momentum thickness Reynolds number
$Re_{\theta,TR}$	momentum thickness Reynolds number at transition
Re_∞	unit free stream Reynolds number (1/m) or (1/ft)
s	streamline distance from stagnation region M_e boundary (m)
s_0	streamline distance from stagnation point (m)
T_e	boundary layer edge temperature (K)

* Aerothermodynamics Branch Senior Technical Lead, AIAA Associate Fellow

$T_{w,AVG}$ average wall temperature (K)
U_e boundary layer edge total velocity (m/s)
U_τ smooth-wall friction velocity
U_∞ free stream velocity (m/s)
(x,y,z) Cartesian coordinates (m)
X_{TR} transition correlation disturbance parameter
Y_{TR} transition correlation flow field parameter
β_N model nose included angle (deg.)
β_{POHL} modified Pohlhausen parameter
δ boundary-layer height (m)
ϕ streamline terminus angular position (deg.)
λ_{POHL} Pohlhausen parameter
ρ_e boundary-layer edge density (kg/m^3)
ρ_∞ free stream density (kg/m^3)
ν_e boundary-layer edge kinematic viscosity (m^2/s)
θ boundary-layer momentum thickness (m)
ϕ streamline angular coordinate identifier
ϕ_{corr} heating calibration corrector factor

II. Background and Introduction

In this work, the effects of distributed sand-grain surface roughness on boundary-layer transition and heating augmentation are considered. Roughness data were obtained through hypersonic wind tunnel testing of a set of representative entry vehicle geometries with roughness patterns that simulated those produced by the ablation of a thermal protection system (TPS). Representative data from this study will be shown herein and the complete data set is presented in detail in Ref [1]. The current test program, in which three-dimensional vehicle geometries are considered, expands on previous investigations [2, 3] of distributed sand-grain roughness effects that was restricted to hemispherical nose-tips. Additionally, the effects of hexcomb pattern roughness on three-dimensional geometries were studied [4, 5] in previous test programs.

"Roughness" is a generic term in aerospace literature that encompasses many types of surface features that deviate from that of a smooth outer mold line (OML). Roughness can be divided into two general types: discrete and distributed. Discrete roughness (Figure 1) includes surface features such as: a) protruding compression pads or recessed cavities at mechanical attachment points; b) steps or gaps between heat shield tiles resulting from differential ablation of the tiles and the filler material between them; and c) physical damage to a TPS. Distributed roughness (Figure 2) includes features such as: a) regular patterns such as those resulting from ablation of hexcomb-structure TPS; b) irregular deflections of a flexible TPS under aerodynamic loading; c) random "sand-grain" features resulting from ablation of a monolithic TPS; or d) the texture of overlapping fibers on a woven TPS.

Data on the effects of surface roughness are valuable because the roughness of an entry vehicle TPS can promote earlier boundary-layer transition and produce higher turbulent heating (and shear) levels than would be expected based on an idealized, smooth-wall analysis. However, due to the complexities of roughness effects, a vehicle's TPS is typically designed using analytical, computational, and/or experimental techniques that are based on the assumption of a smooth surface. The effects of roughness on the aerothermodynamic environment can then be included through approximate engineering correlations and methods.

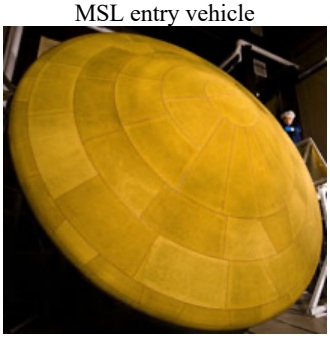
The purpose of this test program was to obtain data on the effects of distributed sand-grain roughness. An example of such sand-grain roughness is shown by a post-flight picture of the Stardust capsule ablated TPS in Figure 3. These data are intended for use in the development and/or validation of engineering correlations for the effects of distributed sand-grain roughness on boundary-layer transition and turbulent heat transfer. They can also serve as the basis for development and/or validation of higher-fidelity, numerical flow-field simulation models for roughness effects.

Heat shield attachment point cavity on Genesis entry vehicle



a) Cavities and protrusions

Block panel layout of TPS on MSL entry vehicle



b) Block TPS steps and gaps

Damaged TPS tiles on Shuttle Orbiter



c) Physical damage to TPS

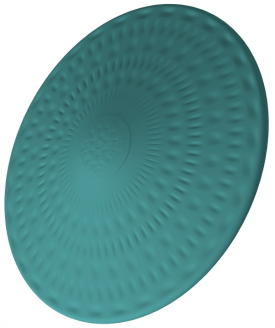
Figure 1. Discrete surface roughness types [Source NASA].

Hexcomb cavities on Apollo ablated TPS



a) Pattern TPS ablation

Flexible TPS deflections over supporting structures



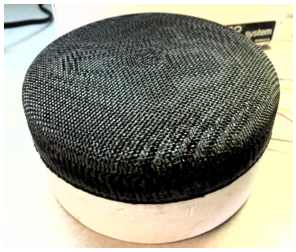
b) Flexible TPS deflections

Ablation of monolithic TPS on Stardust capsule



c) Sand grain TPS ablation

Arc jet test coupon of woven TPS material



d) Woven TPS

Figure 2. Distributed surface roughness types [Source NASA].



Figure 3. Post-flight image of ablated PICA TPS on Stardust entry capsule [Source NASA].

III. Experimental and Computational Methods

A. Wind Tunnel Models

1. Model geometry and fabrication

Roughness effects data were obtained on two representative entry vehicle geometries: a spherical-cap geometry (Figure 4) and a sphere-cone geometry (Figure 5). The spherical-cap geometry is similar to that of the Mercury – Gemini – Apollo – Orion family of entry vehicles employed in the NASA crewed space program. The sphere-cone geometry is similar to that of the Mars Viking – Mars Pathfinder – Mars Exploration Rover – Mars Phoenix – Mars

Science Laboratory – Mars 2020 family of entry vehicle used in the NASA robotic Mars exploration program. Geometric parameters for both configurations are given in the respective figures.

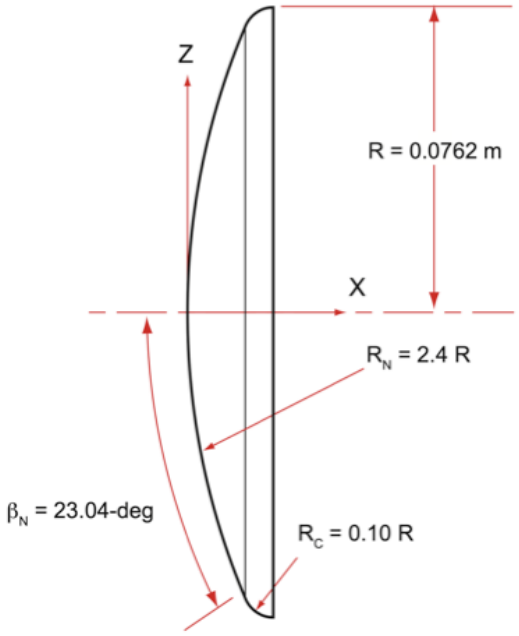


Figure 4. Spherical-cap model geometry.

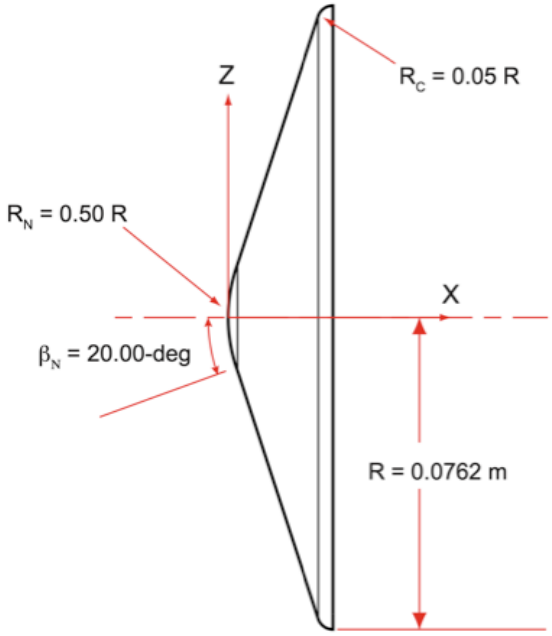


Figure 5. Sphere-cone model geometry.

Multiple models of each configuration were fabricated through ceramic casting with a range of roughness heights. The fabrication process begins with a 3-D printing of a smooth wax pattern of the geometry. An adhesive coating is then applied to the pattern and then it is dipped into a container filled with precision-manufactured, spherical glass particles. The particles adhere to the wax pattern to form a distributed, sand-grain type roughness over the entire surface. The pattern may then be hand-worked if necessary to remove any obvious surface irregularities (i.e., clumps of glass spheres). An investment mold is made from the roughened pattern and a thin-shell ceramic model is then slip cast from the mold, dried, and sintered. The thin-shell is then backfilled with a hydraulically setting magnesia ceramic for strength and support and mounted on a stainless-steel support sting. Finally, the model is coated with a mixture of phosphors that luminesce under ultraviolet lighting and fiducial marks are placed at specified locations on the surface to assist in image registration.

2. Roughness Characterization

The distributed sand-grain surface roughness was created using precision-manufactured, spherical glass particles ranging in size from 2.5 mil to 68.9 mil (note that the "mil" nomenclature, which represents 1/1000 of an inch, is common terminology in roughness studies and will be used herein). The spherical glass particle diameters, D_{ASTM}, are specified according to an ASTM standard [6] that defines a mesh sieve opening size through which the particle can pass. A nominal roughness height for each ASTM mesh size was defined based on the assumption that for a uniform array of roughness elements (the spherical particles) in contact with each other, the roughness height is equal to the vertical distance from the top of an element to the point of contact with the adjacent element as illustrated in Figure 6. Thus, the nominal roughness is simply equal to the particle radius. This height measurement is referred to as the nominal "peak-to-valley" roughness. A listing of the nominal ASTM roughness sizes used in this study is given in Table 1.

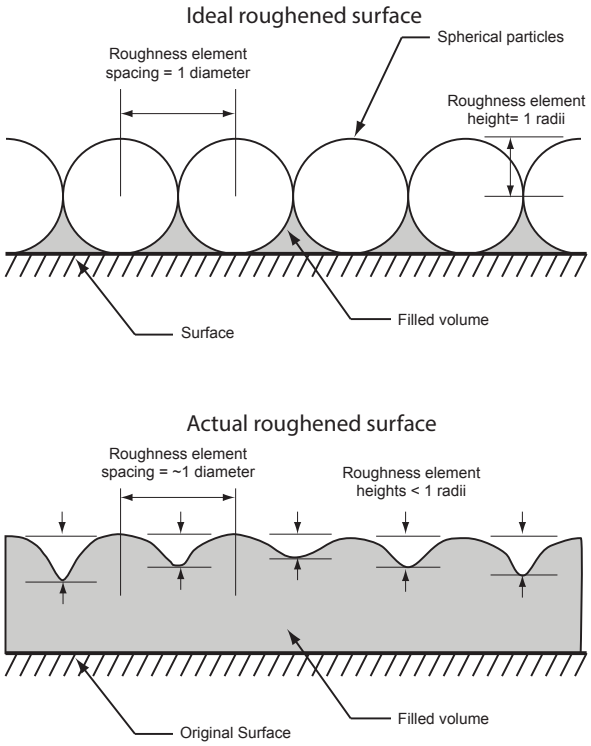


Figure 6. Illustration of ideal and actual surface roughness.

Table 1. Ideal ASTM mesh parameters.

ASTM Mesh Designation	Spherical glass particle diameter, D_{ASTM} (mil)	(mm)	Nominal element height, h_{nom} (mil)	(mm)
ASTM-10	68.90	1.7501	34.45	0.8750
ASTM-20	33.58	0.8529	16.79	0.4265
ASTM-40	16.73	0.1798	8.37	0.0899
ASTM-80	7.09	0.1062	3.54	0.0531
ASTM-140	4.17	0.0630	2.09	0.0315
ASTM-230	2.48	1.7501	1.24	0.8750

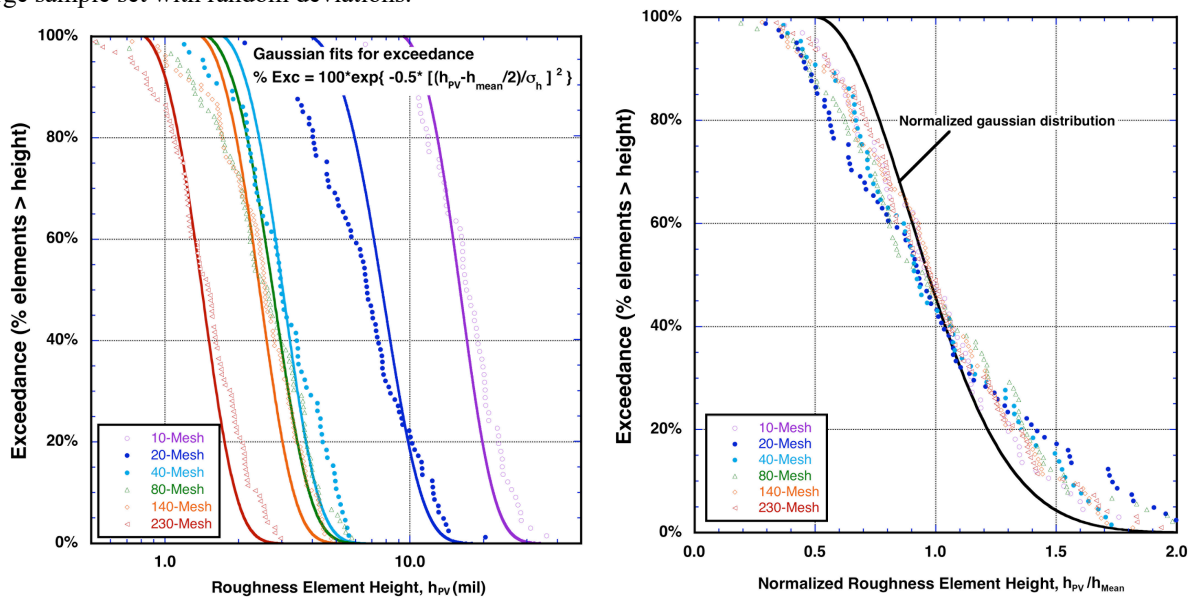
The values in Table 1 represent ideal roughness heights based on the radii of the particles used in the fabrication of each wind tunnel model. However, the characterization of the actual "as-built" roughness was more complex and was based on a statistical analysis of the surface height distributions. The differences between the ideal and as-built roughness geometries are also illustrated in Figure 6. Ideally, in the model fabrication process, the roughness would be defined by perfectly formed hemispherical elements in a single, flat, layer. However, the process of binding the glass particles to the pattern surface, forming the mold, and then casting and coating the ceramic model introduces random imperfections in the surface. To determine the actual roughness values, sample 2-in x 2-in flat plates were cast for each ASTM roughness height, surface image scans were taken, and statistical analyses of the scan data were performed as detailed in Ref. [1]. The scan data were processed to determine several parameters, including the root-mean-square surface height distribution (h_{RMS}), local peak-to-valley roughness element heights (h_{PV}), and the actual effective peak-to-valley roughness height (k_{PV}). These definitions are summarized below and more detail is provided in Ref. [1].

The root mean square height distribution, h_{RMS}, is a function of the distribution of all height measurement points over the *entire* sample surface as per Eq. (1), where n is the number of measurement points and z_i is the point height above a reference plane. This RMS value does not provide a direct characterization of the roughness element heights, since measurement locations do not necessarily coincide with the maximum or minimum of an individual roughness

element. Nevertheless, the RMS height is a relatively straightforward quantity to define and measure and is frequently reported in roughness studies.

$$h_{RMS} = \sqrt{\frac{1}{n}\sum_{i}(z_i)} \tag{1}$$

The peak-to-valley roughness height, h_{PV}, provides a better definition of the dimensions of a roughness element and is defined as the difference between the maximum and minimum height of an element. Because the actual peak-to-valley values vary over the surface, a statistical analysis of the data was performed. First, profile lines were extracted from the scan data for each flat plate and the peak and valley heights of individual elements were tabulated. From these tabulations, the statistical exceedance, which is defined as the percentage of data points in a set greater than a specified value, was computed. These exceedance height distributions obtained from scans of each sample plate are plotted in Figure 7a. Also shown in this figure are Gaussian curve fits to these data of the form given by Eq. (2), where h_{mean} is the mean of the measured peak-to-valley heights and σ_h is the standard deviation. The exceedance height distributions are replotted in terms of the normalized roughness height (h_{PV}/h_{mean}) in Figure 7b. As seen in these two figures, the exceedance distributions approximate the Gaussian distribution that would be expected from a large sample set with random deviations.



a) Individual data sets **b) Normalized data**

Figure 7. Exceedance distributions for roughness sample plates.

$$\text{Exceedance}_{\text{Gaussian}} = 100\% \times exp\{-0.5[(h_{PV} - h_{mean}/2)/\sigma_h]^2\} \tag{2}$$

An additional complication in roughness height measurements is the difference between the actual peak-to-valley height of a roughness element and the value measured along a profile line, which does not necessarily pass through the center of a given roughness element. A relationship between the statistical mean of measured roughness heights, h_{mean}, and the actual roughness height, k, was developed by Dirling [7] in an analysis for simple geometric elements including hemispheres, cones and rectangles. For the purposes of this study, it was assumed that Dirling's analysis for the mean value also holds for any arbitrary exceedance percentile value, allowing for estimation of the true peak-to-valley exceedance height, k_{PV}, values from the heights, h_{PV}, measured along the profile lines. Dirling's function, as given by Eq. (3), employs a transfer function, p_{trans}, to relate the actual and measured roughness heights. The $\pi/4$ value of the transfer function was employed as the distributed sand-grain roughness elements in this study can be approximated as a tightly packed array of nominally hemispherical elements.

A final complexity in the determination of roughness heights is that the nominal values of the higher ASTM particles (80 ASTM and greater) were smaller than the optical resolution of the scanner used to gather roughness data. As detailed in Ref. [1], the relationship between nominal and peak-to-valley exceedance heights for higher ASTM sizes (smaller particle diameters) was inconsistent with those for the smaller ASTM sizes (larger particle diameters). Thus, an empirical correction was applied to the high ASTM size samples. The nominal heights, measured RMS values, and the original and corrected values for the 50% peak-to-valley roughness heights are all given in Table 2.

$$h_{PV} = k_{PV} \times p_{trans}: \text{where } p_{trans} = \begin{cases} \pi/4 & \text{hemispherical element} \\ 0.5 & \text{conical element} \\ 1 & \text{rectangular element} \end{cases} \tag{3}$$

Table 2. Model roughness information.

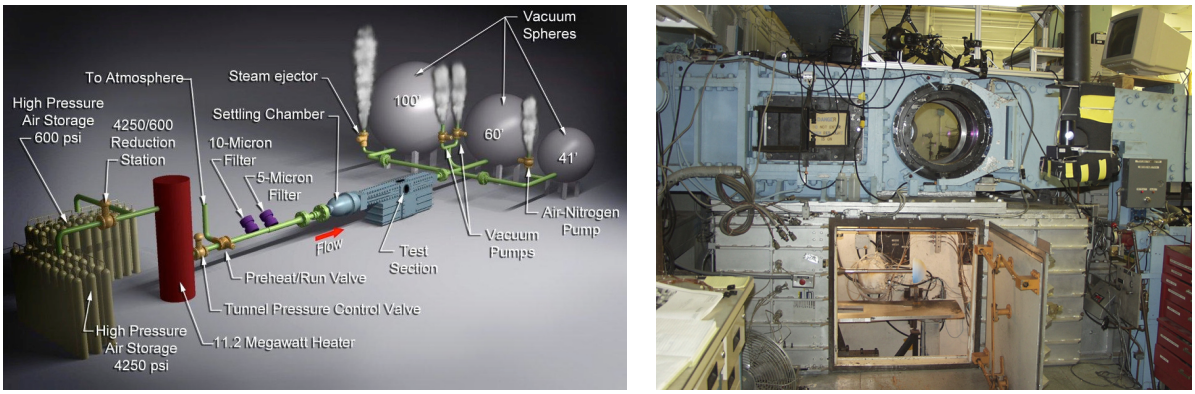
ASTM Mesh	Nominal Height h (mil)	Nominal Height h (mm)	Measured RMS height h_{RMS} (mil)	Measured RMS height h_{RMS} (mm)	Original 50% exceedance k_{PV50} (mil)	Original 50% exceedance k_{PV50} (mm)	Corrected 50% exceedance k_{PV50} (mil)	Corrected 50% exceedance k_{PV50} (mm)
10	34.45	0.8750	7.873	0.2000	21.48	0.5456	N/A	N/A
20	16.79	0.4265	2.380	0.0605	8.49	0.2156	N/A	N/A
40	8.37	0.2126	1.430	0.0363	3.83	0.0973	N/A	N/A
80	3.54	0.0899	1.181	0.0300	3.40#	0.0864#	2.63	0.0668
140	2.09	0.0531	1.102	0.0280	3.21#	0.0815#	2.15	0.0546
230	1.24	0.0315	0.683	0.0173	1.94#	0.0493#	1.29	0.0328
Smooth	N/A	N/A	0.500	0.0127	1.46#	0.0371#	0.98	0.0249

denotes a value corrected due to lack of scan precision

B. Wind Tunnel Test Facility and Operating Conditions

3. Facility Description

Wind tunnel testing was performed in the 20-Inch Mach 6 Air Tunnel of the NASA Langley Aerothermodynamics Laboratory (LAL). The 20-Inch Mach 6 Air Tunnel (Figure 8) is a blow-down to vacuum facility in which heated, dried, and filtered air is used as the test gas. The tunnel has a two-dimensional contoured nozzle that opens into a 20.5 in. × 20.0 in. test section. The tunnel is equipped with a bottom-mounted injection system with a -5 deg. to +55 deg. pitch range and ±5 deg. yaw range that can transfer a model from a sheltered model box to the tunnel centerline in less than 0.5 sec. Run times of up to 15 minutes are possible in this facility, although for aeroheating studies, run times of only a few seconds are typically required. The nominal reservoir conditions of this facility produce perfect-gas free stream flows with Mach numbers between 5.8 and 6.1 and unit Reynolds numbers of 0.5×10^6/ft to 8.3×10^6/ft. With its wide Reynolds number operating range capable of producing laminar, transitional, or turbulent flow on most geometries, this tunnel is primarily used for heat-transfer and boundary-layer transition studies. More detailed information on this and other LAL facilities can be found in Refs. [8–9].



a) Schematic **b) Test section [source NASA]**

Figure 8. Langley Research Center 20-Inch Mach 6 Air Tunnel.

4. Facility Operating Conditions

Data were obtained during Tests 7036 and 7057 in the 20-Inch Mach 6 Air Tunnel at six unit Reynolds numbers from $Re_\infty = 2.1\times10^6$/ft to 8.1×10^6/ft. All spherical-cap data were obtained at $\alpha = 28$ deg. and all sphere-cone data were obtained at $\alpha = 16$ deg. The angles of attack were chosen for continuity with smooth-OML data obtained in prior testing of the these geometries [4-5]. Free stream values for velocity (U_∞), density (ρ_∞), temperature (T_∞), unit Reynolds number (Re_∞), and Mach number (M_∞) for the test conditions are listed in Table 3. Additionally, the enthalpy difference (ΔH_{tot}), and reference heat transfer film-coefficient value (h_{FR}) are provided. The enthalpy term is defined as the difference $H_0 - H_{300K}$ between the free stream total enthalpy and the wall enthalpy at cold wall (300 K) conditions. The film coefficient is the value from the Fay-Riddell theory [10] for a hemispherical radius at cold wall (300 K) conditions, where the radius is the nose radius of the respective model geometry.

Table 3. Nominal 20-Inch Mach 6 Air Tunnel Conditions.

Re_∞ (1/ft)	Re_∞ (1/m)	M_∞	T_∞ (K)	ρ_∞ (kg/m^3)	U_∞ (m/s)	ΔH (J/kg)	h_{FR} (kg/m^2-s) spherical-cap	h_{FR} (kg/m^2-s) sphere-cone
2.051E+06	6.725E+06	5.968	62.94	3.203E-02	948.4	2.121E+05	1.144E-01	2.536E-01
2.992E+06	9.816E+06	5.998	63.26	4.666E-02	955.1	2.187E+05	1.401E-01	3.072E-01
4.966E+06	1.629E+07	6.030	63.72	7.741E-02	962.9	2.266E+05	1.824E-01	3.992E-01
6.489E+06	2.129E+07	6.042	63.48	1.008E-01	962.1	2.256E+05	2.078E-01	4.555E-01
7.199E+06	2.362E+07	6.047	63.48	1.118E-01	962.7	2.261E+05	2.189E-01	4.800E-01
8.136E+06	2.669E+07	6.034	59.21	1.224E-01	924.9	1.860E+05	2.180E-01	4.781E-01

C. Experimental Data Acquisition and Reduction

1. Data Acquisition and Reduction

Experimental data were obtained using the two-color, relative-intensity, global phosphor thermography method [11, 12] and reduced using the IHEAT (Imaging for Hypersonic Experimental Aerothermodynamic Testing) code [13]. In this method, a model is illuminated by ultraviolet light sources that induce temperature-dependent fluorescence of the phosphor coating. Fluorescent intensity images of a model are taken in the tunnel before and during a run using a three-color, charge-coupled device camera. The intensity data are converted to temperature using pretest calibrations of the data acquisition system and the temperature data are then processed to determine heat-transfer distributions.

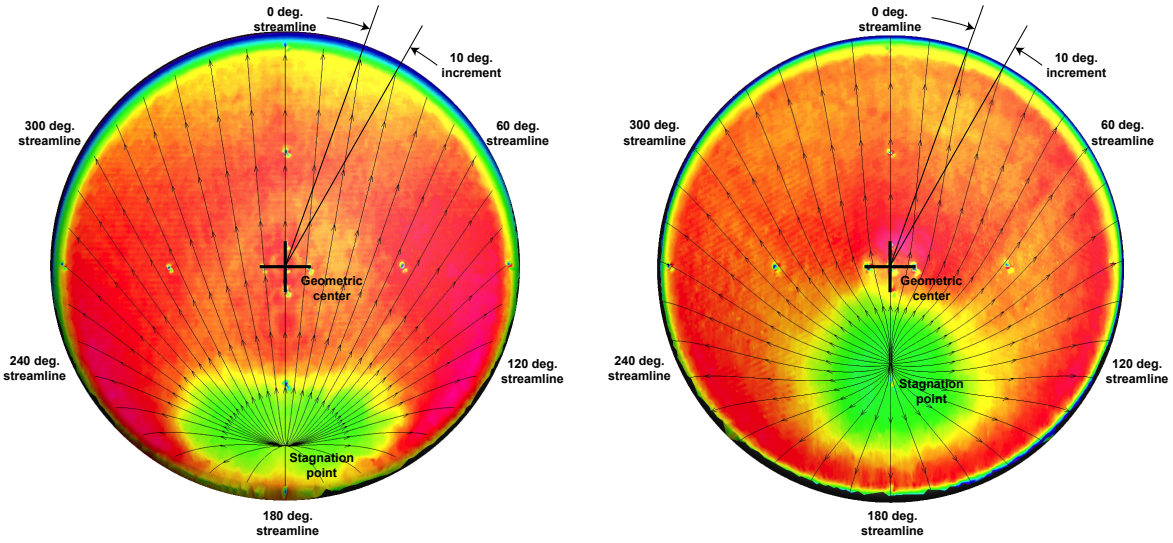
Heat-transfer film coefficients are determined by assuming a step function in the film coefficient from the prerun temperature to the run temperature, which corresponds to an assumed parabolic temperature-time history. The heating data are typically reported in terms of the ratio h/h_{FR} where the heat-transfer film coefficient, h, is defined in terms of enthalpy as $h = q/(H_{AW} - H_w) = q/(H_0 - H_w)$. In the calculation of the heat-transfer film coefficient, it is assumed that, for a blunt-body, the adiabatic wall enthalpy H_{AW} is equal to the free stream total enthalpy of the tunnel, H_0. This heat transfer coefficient definition provides a theoretically near-constant value over the course of a run since the decrease in time of the heat transfer rate in the numerator as the model surface becomes hotter is balanced by the decrease of the enthalpy-difference term in the denominator.

2. Data Mapping and Presentation

The two-dimensional (2-D) image data output from IHEAT for each run were transformed to account for optical perspective effects and mapped to a three-dimensional (3-D) CAD surface of the wind tunnel model. To accomplish this mapping, perspective, translational, and rotational transformations were first performed on the 3-D CAD surface until its 2-D projection matched that of the 2-D image data. The image data were then assigned transformed (x, y, z) coordinates based on interpolation between the image and surface geometry. Finally, the transformation was inverted to obtain an orthographic, 3-D heating distribution map of the experimental data.

An additional data manipulation was performed to extract the streamline-based heating distributions from the mapped wind tunnel data set. These streamline-based data sets are used in boundary-layer transition analyses and for comparisons of Reynolds number and roughness height effects. For each run, streamlines were defined based on the boundary-layer edge velocity vectors from the computed flow fields (to be discussed in the next section). Thirty-six streamline termini were established at locations spaced in 10 deg. increments around the circumference of the geometry and the streamlines were then traced backward from each terminus toward the flow field stagnation point. Each streamline is identified by the angular location, ϕ, of its terminus.

The resulting streamlines are shown in Figure 9a for the spherical-cap geometry and in Figure 9b for the sphere-cone geometry. The geometric definition (*x, y, z*) of each streamline was interpolated onto the 3-D mapped images and then data were extracted along each streamline in terms of h/h_{FR} vs. s/R, where s/R is the normalized streamline distance from the stagnation point. Additionally, the predicted flow field quantities (boundary-layer height, momentum-thickness Reynold number, etc.) were also extracted along these streamlines and combined with the experimental data set to enable transition onset analyses.



a) Spherical-cap geometry **b) Sphere-cone geometry**

Figure 9. Streamlines for data extraction.

3. Experimental Uncertainty

The experimental uncertainty for convective heat transfer measurements on a smooth, blunt body geometry model in the 20-Inch Mach 6 Air Tunnel is quantified as a function of net uncertainties resulting from: the data acquisition method (±10%); flow quality and test-condition repeatability (±5%); and the accuracy of the 3D mapping process (±10%), which results in an overall root-sum-squared value of ±15%. Experience with this technique indicates that these values are usually conservative and as will be shown later, the predicted and measured heating distributions were in close agreement (generally less than ±5%) for laminar, smooth-wall cases. It is assumed that the sand-grain roughness patterns introduced additional uncertainties because they produced very detailed heating patterns which, in some cases, were smaller than the resolution of the camera system. Thus, a measurement in such areas is, in effect, a spatial average rather than a point measurement. Quantification of such errors on a macro-scale is not possible because of the localized and position/pattern dependency of roughness features, but is probably on the order of ±10–20%. Taken together with the smooth-wall uncertainty, the uncertainty in distributed sand-grain roughness heating is estimated to be in the ±18–25% range.

An additional factor that influences the quality of phosphor thermography data quality is the local surface inclination at a given point on the model with respect to both the camera and the illumination source. Phosphor thermography provides the best result when the surface to be imaged is normal to the camera, which reduces perspective distortion and image smearing, and when the surface is well illuminated by the ultraviolet lights, which induces the best temperature response of the phosphor coating. Because of the three-dimensional nature of a wind tunnel model, its entire surface cannot be optimally imaged, or in some cases cannot even be viewed. For blunt bodies such as those in this test, the windward centerline region of the model – the 'bottom' of the model with respect to the view orientation – is the area where the data quality was most affected. This situation is illustrated for a simple hemispherical geometry in Figure 10. Because of this limitation, windward centerline region data are only regarded as qualitative, not quantitative. Although image data from this region will be shown, quantitative plotted data and transition location data will not be provided for the streamlines originating from the 160 deg. through 200 deg. termini.

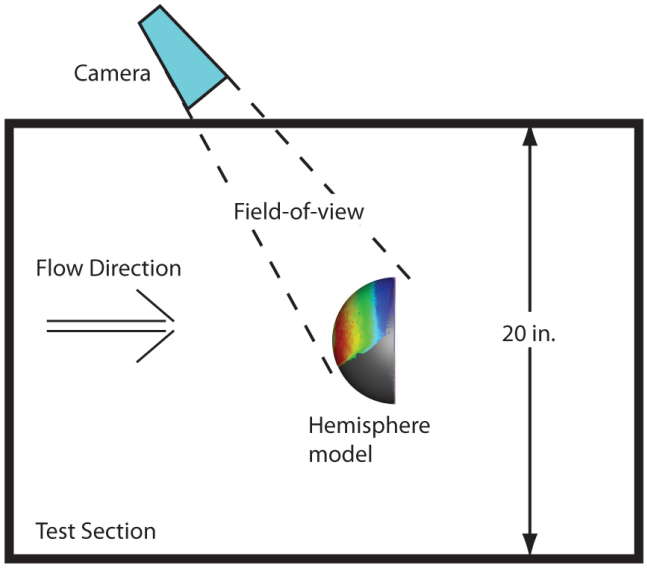


Figure 10. Illustration of camera field-of-view for hemisphere model in 20-Inch Mach 6 Air Tunnel.

D. Computational Tools and Methods

Flow field solutions were generated using the LAURA (Langley Aerothermodynamic Upwind Relaxation Algorithm) code. LAURA [14-15] is a three-dimensional, structured-grid, finite-volume solver that includes perfect-gas and nonequilibrium chemistry options, a variety of turbulence models, and ablation and radiative transport capabilities. LAURA solutions were used for comparisons of predicted heating levels with the measured data and to define the streamlines along which to extract the mapped experimental data, as described above.

Solutions were computed on multiblock grids of each geometry with a smooth (no surface roughness) outer mold line. Grid adaption was performed to align the grid outer boundary with the bow shock and to cluster cells near the surface to produce wall cell Reynolds numbers on the order of 1 to 10. Free stream conditions were set to the nominal wind tunnel conditions for each run as given in Table 3. For these wind tunnel conditions, the perfect-gas air option was used. Both laminar and turbulent solutions were generated. Turbulent cases were computed using the Cebeci-Smith algebraic model with fully-turbulent flow over the entire geometry.

For the wall temperature boundary condition, a change in the normal practice for wind tunnel simulations of setting this value to a "cold-wall" ambient temperature (because of the usually small variation in heat-transfer coefficient with temperature) was employed. Literature on roughness effects indicates a dependence of transition onset location on the ratio of boundary-layer edge temperature to wall temperature T_e/T_w. To approximately account for this effect (which was expected to be small for these test conditions), the computations were performed using a uniform "hot-wall" wall temperature set to the average of the measured surface temperature on the model. These values varied between 327 K to 411 K, depending on roughness height and test condition. These hot-wall temperatures are listed for each run in Ref. [1].

IV. Experimental Results

A. Reynolds Number Effects on Heating and Transition

The effects of Reynolds number on the heating levels and boundary-layer transition onset locations are illustrated for the baseline smooth surface spherical-cap model in Figure 11 –

Figure 12 and for the baseline smooth sphere-cone model in Figure 13 - Figure 14. Two figures are provided for each model: line plots of h/h_{FR} vs. s/R are shown in the first figure and global heating images are shown in the second. For brevity, all streamlines are not shown in these figures; instead, streamlines are shown at 30 deg. increments from 0 deg. to 150 deg. As noted earlier, the data for streamlines between 160 deg. and 200 deg. are considered to be qualitative, not quantitative. Data for streamlines from 210 deg. to 360 deg. are nominally symmetric with the data from 0 deg. to 150 deg., although in practice, model surface irregularities can cause asymmetric behavior. Such local asymmetries can be observed in the images that accompany the line plots. In general, the flow remained laminar on

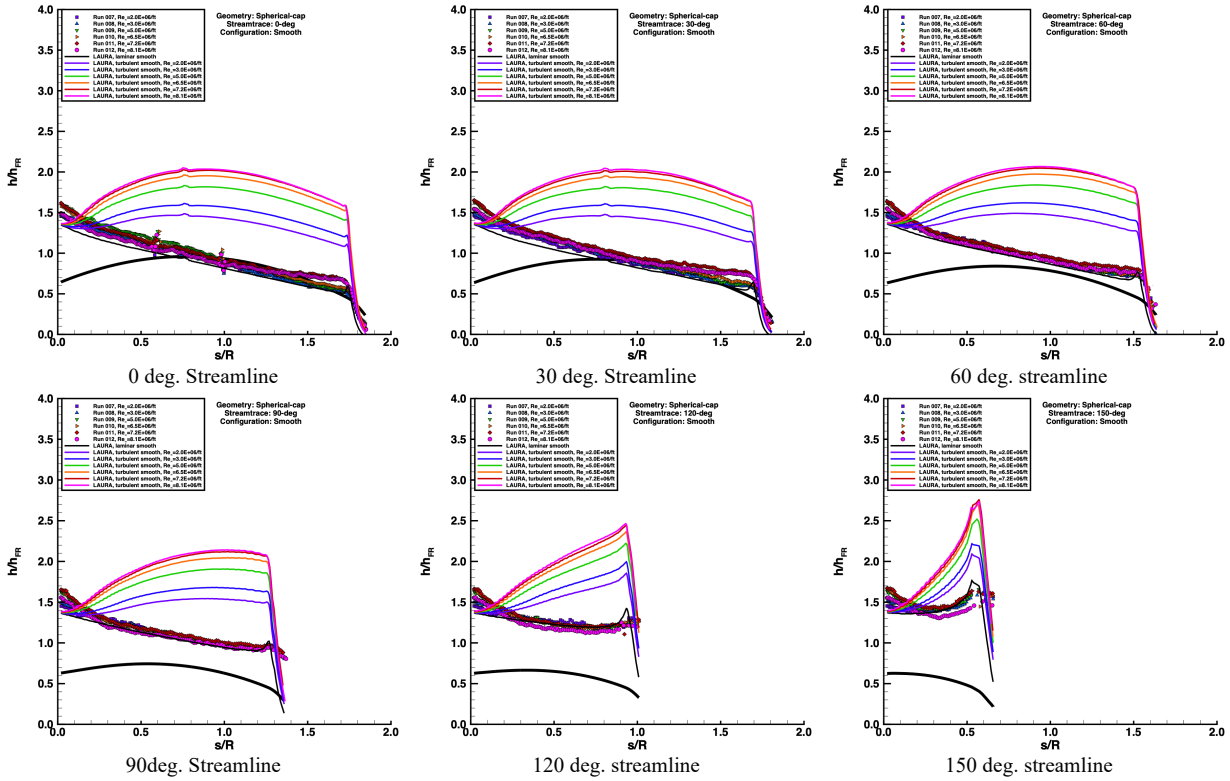
both smooth model geometries for the majority of test conditions. However, small transitional/turbulent wedges were produced on the sphere-cone model at the higher Reynolds numbers.

A sample set of figures for the ASTM-80 model sand-grain roughness data is shown in Figure 15 - Figure 16 for the spherical cap and in Figure 17 - Figure 18 for the sphere-cone. For brevity, the results from the other configurations are omitted, but they can be found in Ref. [1]. As expected, the sand-grain roughness produced earlier boundary-layer transition than was observed on the smooth model. Additionally, the heating levels downstream of transition were higher than those from the smooth-wall turbulent heating predictions.

In these line-plots, the LAURA predictions for smooth-wall, laminar and turbulent heating levels are also shown. Because the heat-transfer film coefficient ratio, h/h_{FR}, remains nearly constant with Reynolds number, only the lowest Reynolds number laminar prediction is included for each model. However, since this invariance does not hold for turbulent flow, turbulent predictions are shown for all Reynolds numbers. As noted previously, turbulent cases were modeled as fully-turbulent flow over the entire geometry. These turbulent cases are shown as limiting bounds, since the actual transition occurred at different locations for each test condition / model geometry. Agreement to within or less than the experimental uncertainty between the laminar predictions and the laminar data was observed for all cases except at the transitional/turbulent wedges for the higher Reynolds number sphere-cone model cases.

B. Configuration Effects on Heating and Transition

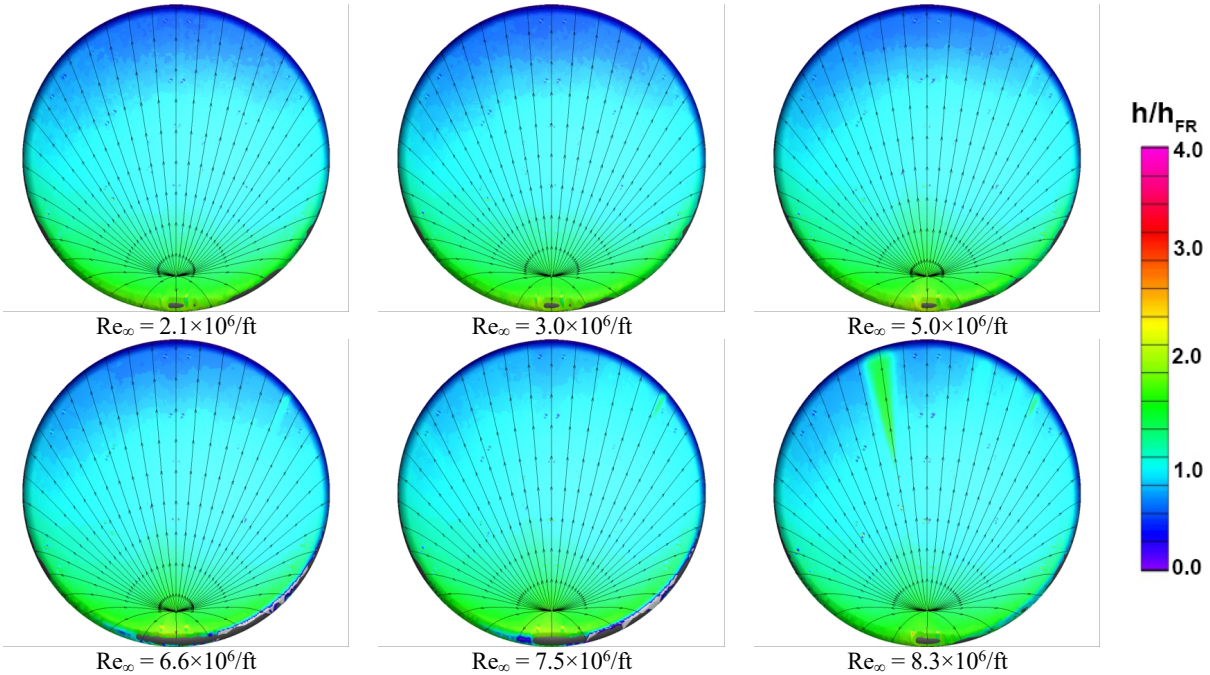
The effects of the roughness height on heating levels and boundary-layer transition are shown for sample cases in Figure 19 - Figure 20 for the spherical-cap geometry and in Figure 21 - Figure 22 for the sphere-cone geometry. These examples are for the $Re_\infty = 5.0\times10^6$/ft condition. Results for the other Reynolds numbers can be found in Ref. [1]. As expected, increasing the roughness height caused transition to move upstream and caused the turbulent heating augmentation to increase.



0 deg. Streamline | 30 deg. Streamline | 60 deg. streamline

90deg. Streamline | 120 deg. streamline | 150 deg. streamline

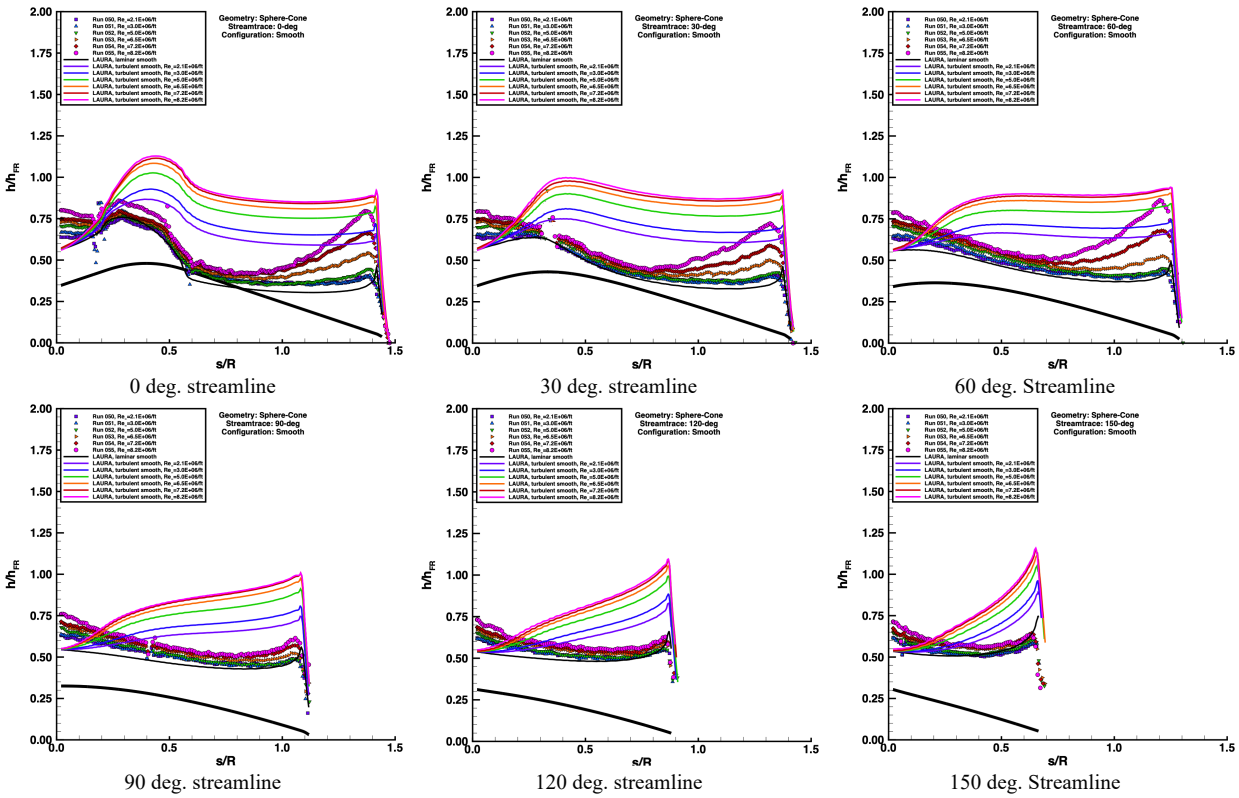
Figure 11. Reynolds Number effects, spherical-cap smooth model plots.



$Re_\infty = 2.1\times10^6$/ft | $Re_\infty = 3.0\times10^6$/ft | $Re_\infty = 5.0\times10^6$/ft

$Re_\infty = 6.6\times10^6$/ft | $Re_\infty = 7.5\times10^6$/ft | $Re_\infty = 8.3\times10^6$/ft

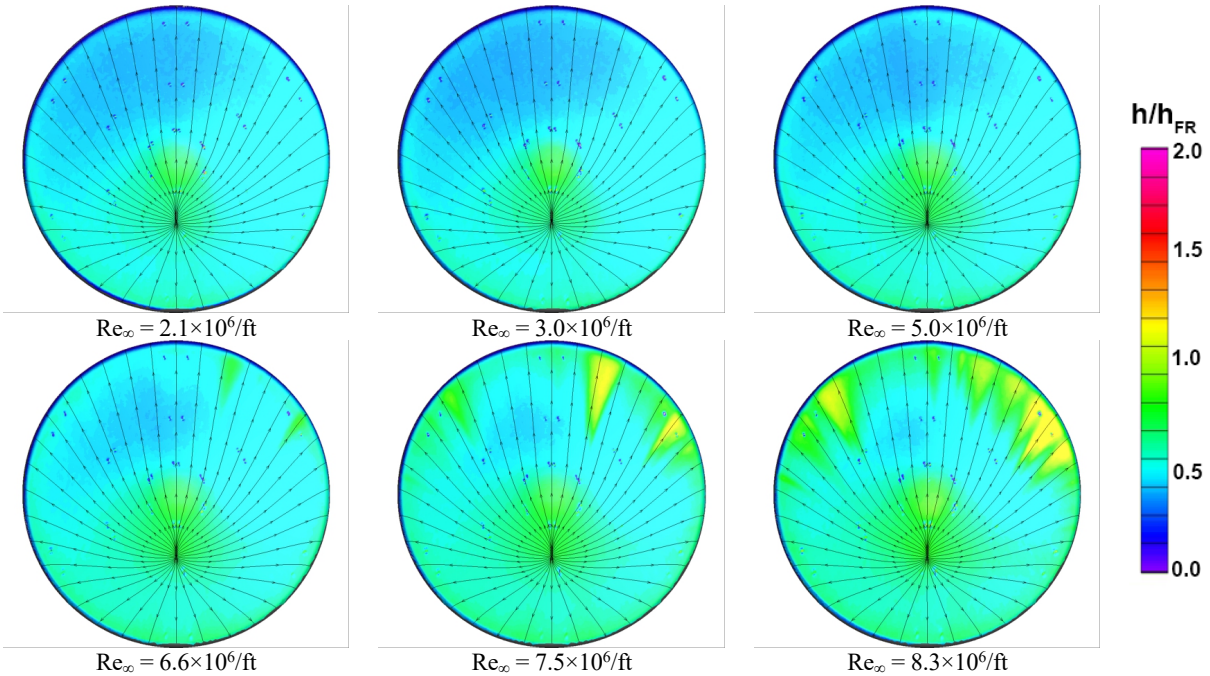
Figure 12. Reynolds Number effects, spherical-cap smooth model images.



0 deg. streamline | 30 deg. streamline | 60 deg. Streamline

90 deg. streamline | 120 deg. streamline | 150 deg. Streamline

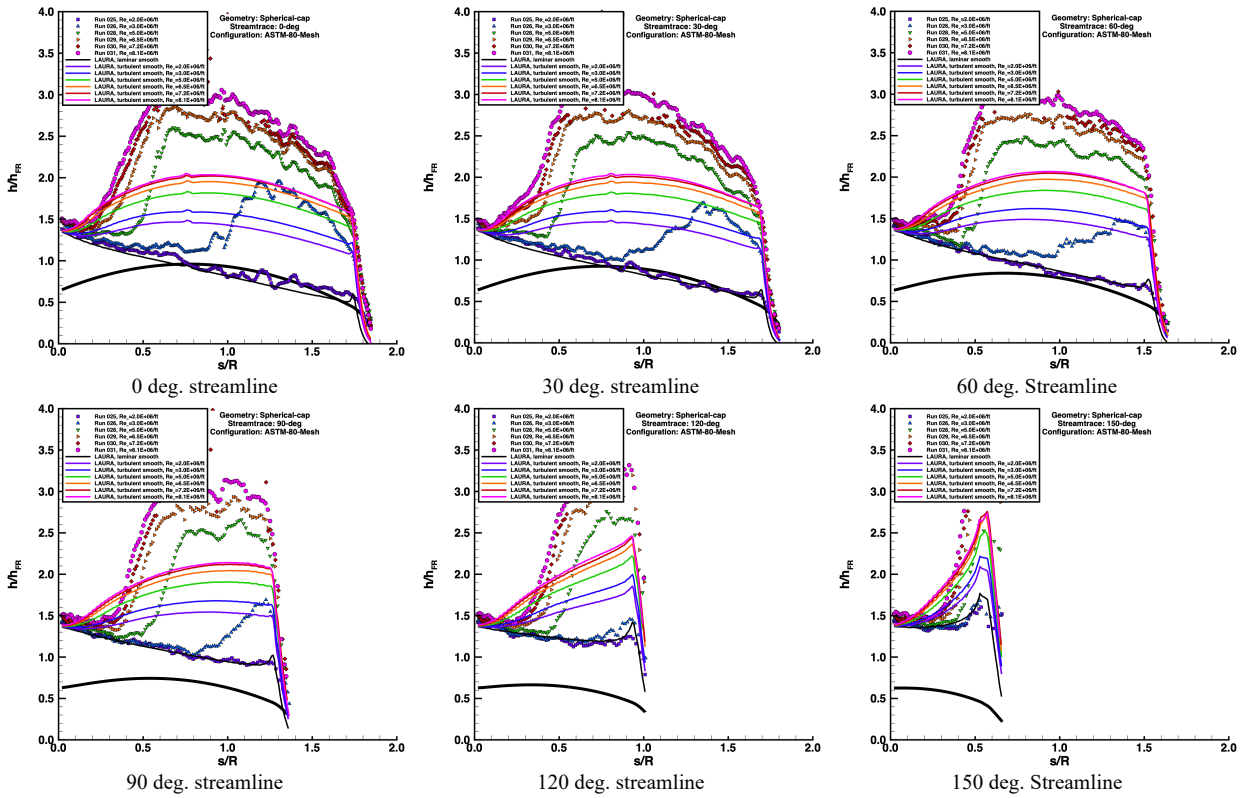
Figure 13. Reynolds Number effects, sphere-cone smooth model plots.



$Re_\infty = 2.1\times10^6$/ft | $Re_\infty = 3.0\times10^6$/ft | $Re_\infty = 5.0\times10^6$/ft

$Re_\infty = 6.6\times10^6$/ft | $Re_\infty = 7.5\times10^6$/ft | $Re_\infty = 8.3\times10^6$/ft

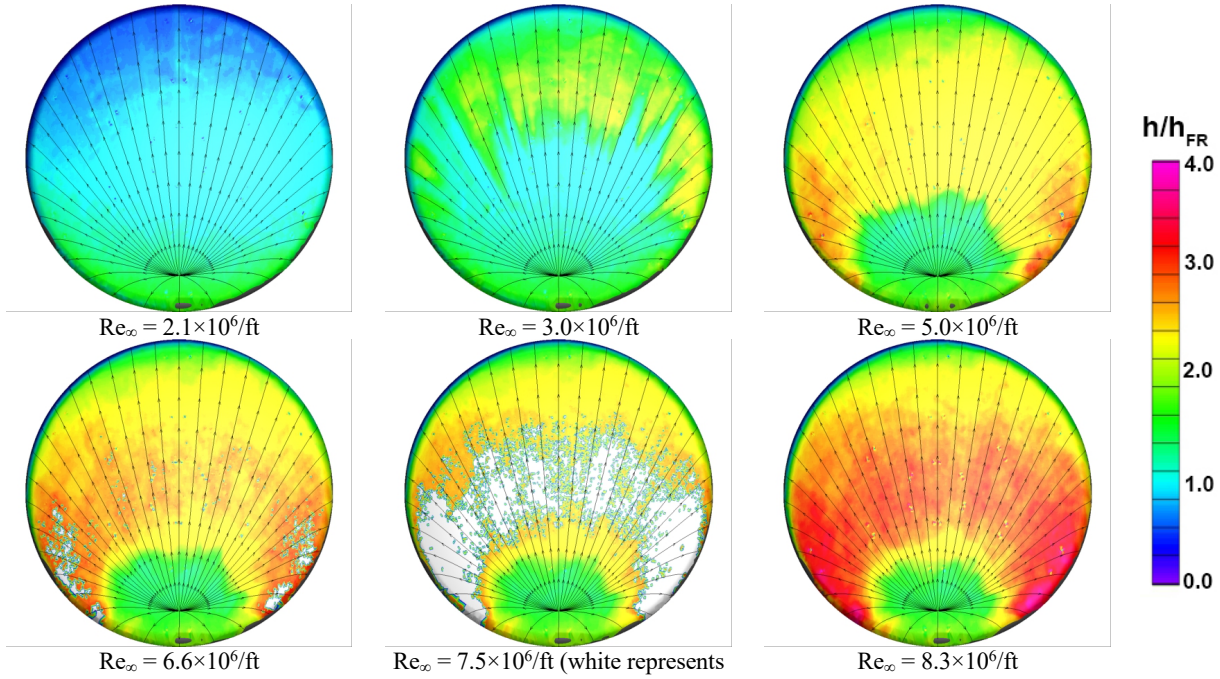
Figure 14. Reynolds Number effects, sphere-cone smooth model images.



0 deg. streamline | 30 deg. streamline | 60 deg. Streamline

90 deg. streamline | 120 deg. streamline | 150 deg. Streamline

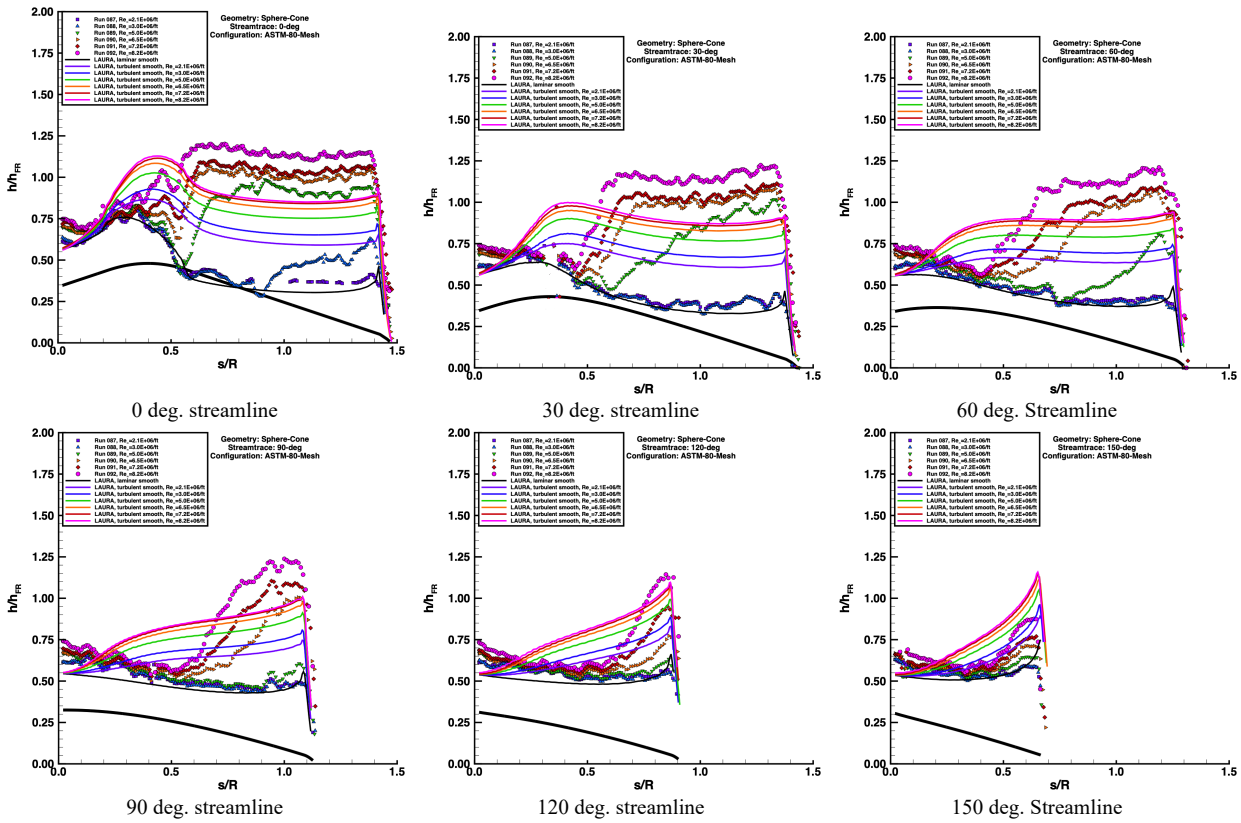
Figure 15. Reynolds Number effects, spherical-cap ASTM-80 model plots.



$Re_\infty = 2.1\times10^6$/ft | $Re_\infty = 3.0\times10^6$/ft | $Re_\infty = 5.0\times10^6$/ft

$Re_\infty = 6.6\times10^6$/ft | $Re_\infty = 7.5\times10^6$/ft (white represents wall temperatures off-scale) | $Re_\infty = 8.3\times10^6$/ft

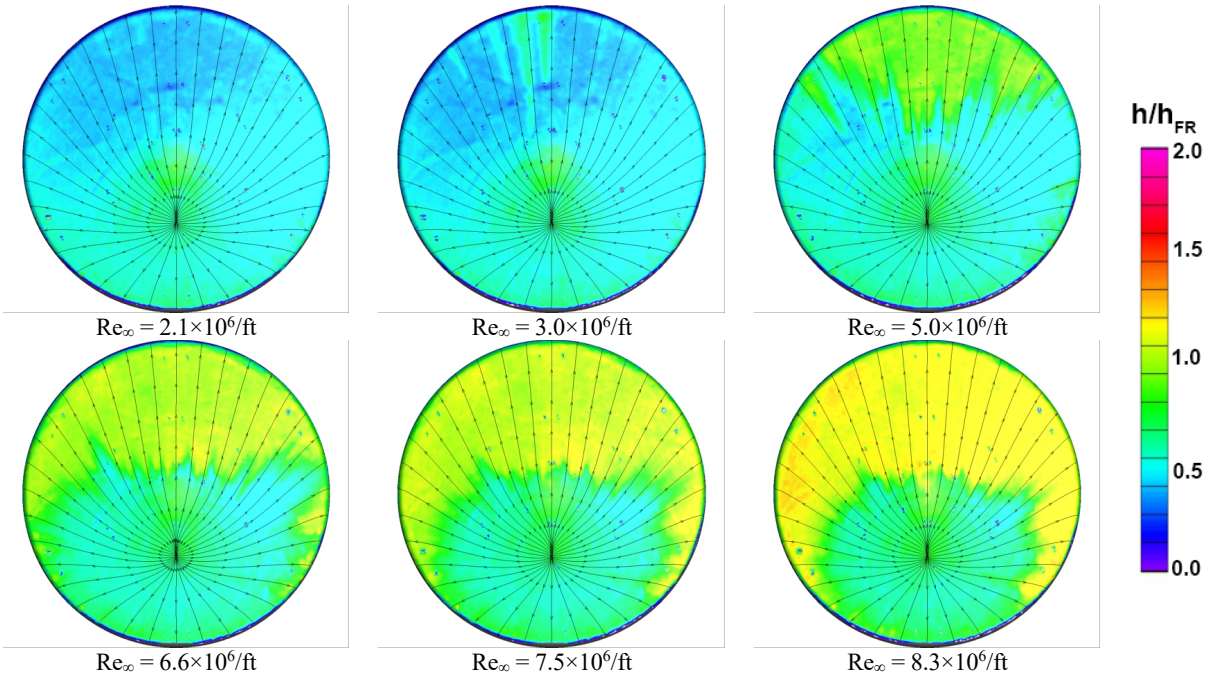
Figure 16. Reynolds Number effects, spherical-cap ASTM-80 model images.



0 deg. streamline | 30 deg. streamline | 60 deg. Streamline

90 deg. streamline | 120 deg. streamline | 150 deg. Streamline

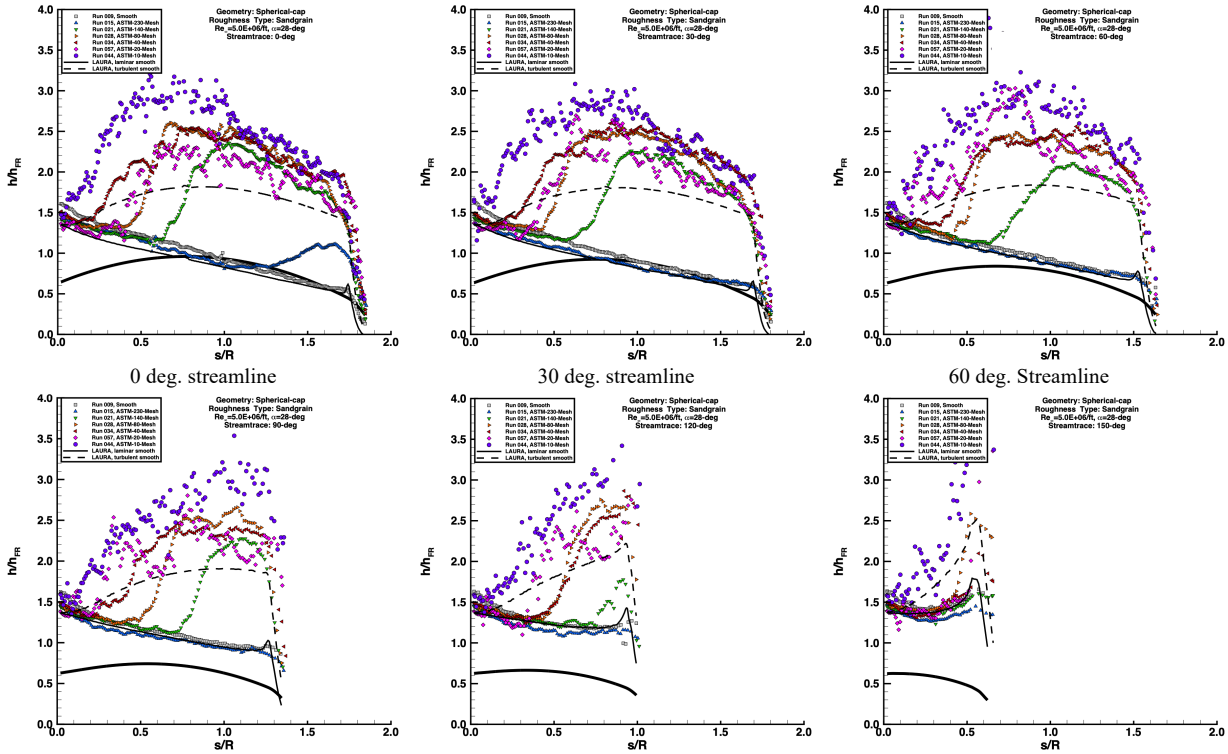
Figure 17. Reynolds Number effects, sphere-cone ASTM-80 model plots.



$Re_\infty = 2.1\times10^6$/ft | $Re_\infty = 3.0\times10^6$/ft | $Re_\infty = 5.0\times10^6$/ft

$Re_\infty = 6.6\times10^6$/ft | $Re_\infty = 7.5\times10^6$/ft | $Re_\infty = 8.3\times10^6$/ft

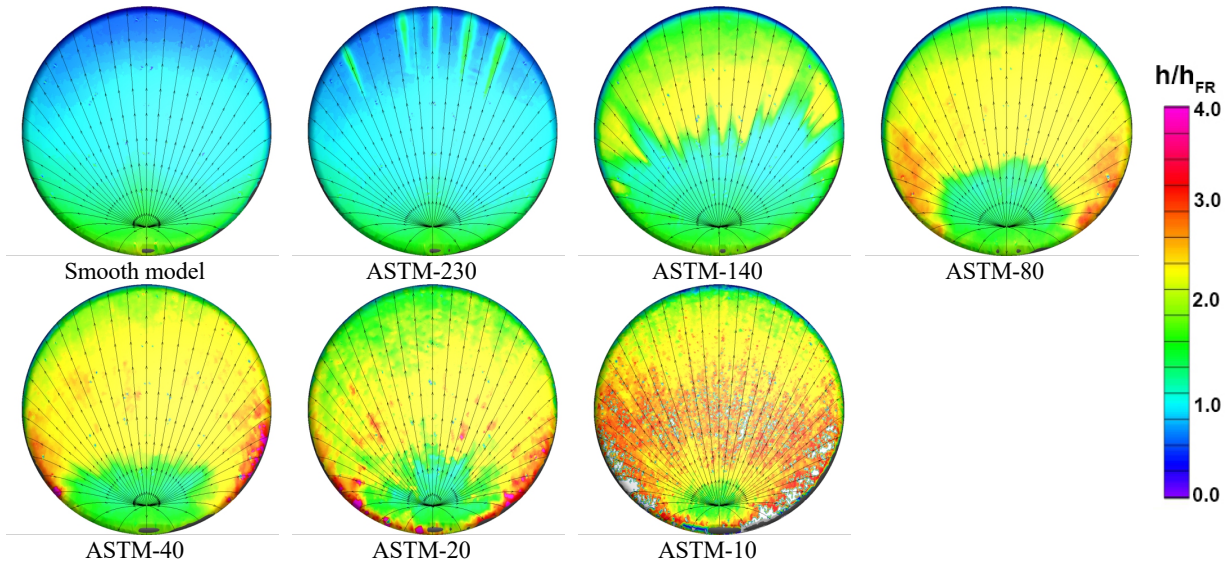
Figure 18. Reynolds Number effects, sphere-cone ASTM-80 model images.



0 deg. streamline 30 deg. streamline 60 deg. Streamline

90 deg. streamline 120 deg. streamline 150 deg. Streamline

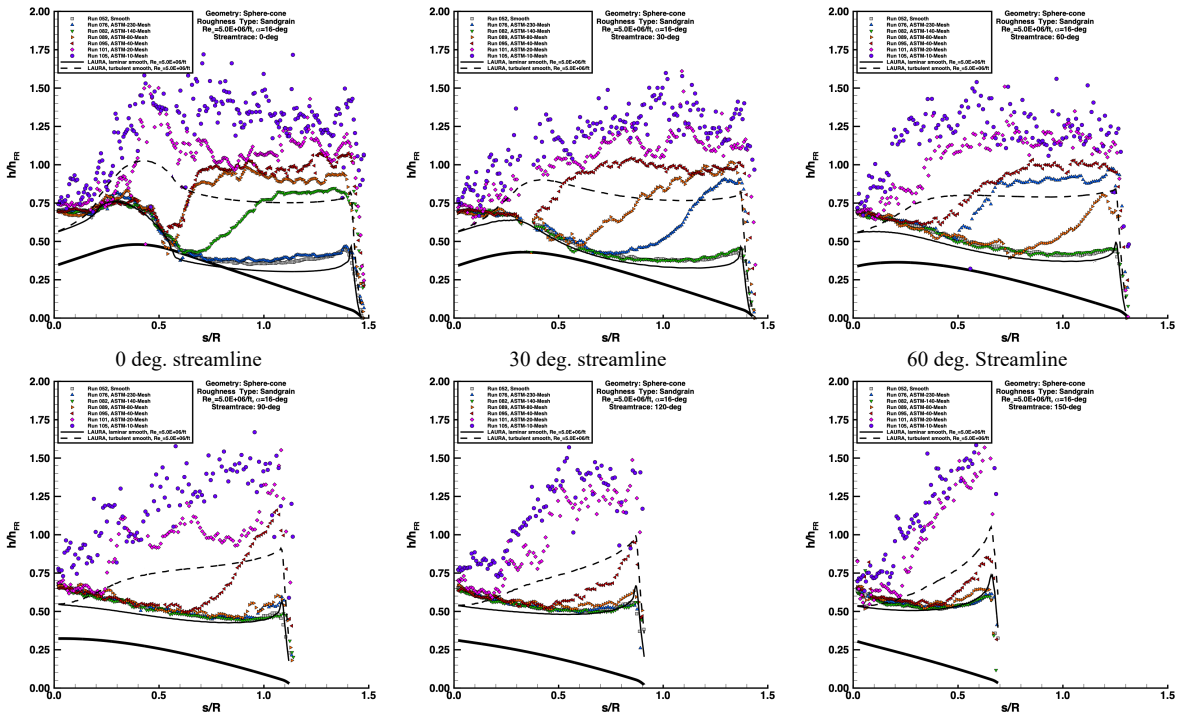
Figure 19. Roughness height effects, spherical-cap geometry, $Re_\infty = 5.0\times10^6$/ft plots.



Smooth model ASTM-230 ASTM-140 ASTM-80

ASTM-40 ASTM-20 ASTM-10

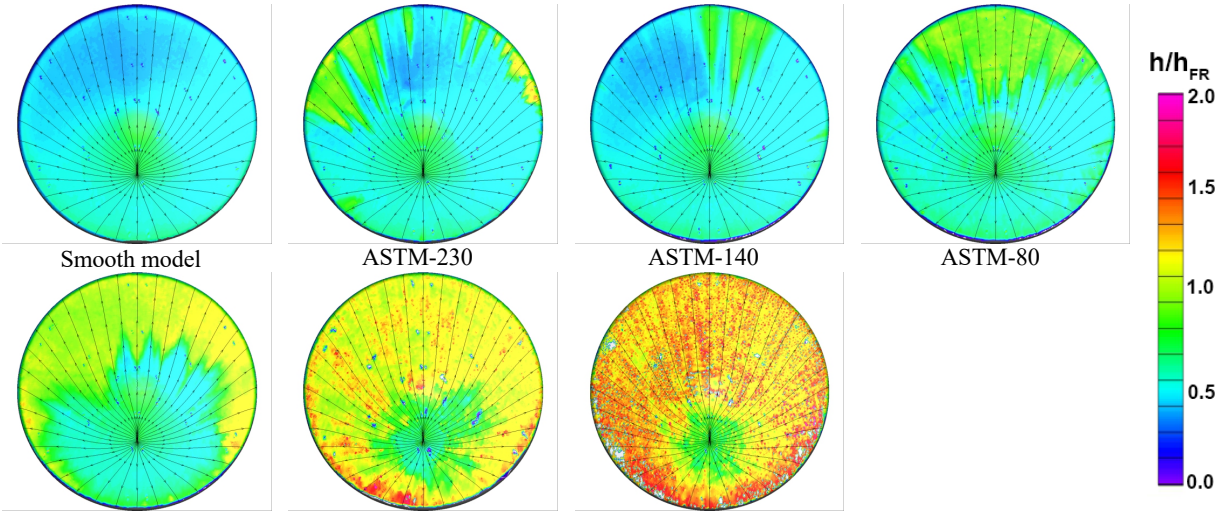
Figure 20. Roughness height effects, spherical-cap geometry, $Re_\infty = 5.0\times10^6$/ft images.



0 deg. streamline | 30 deg. streamline | 60 deg. Streamline

90 deg. streamline | 120 deg. streamline | 150 deg. streamline

Figure 21. Roughness height effects, sphere-cone geometry, $Re_\infty = 5.0\times10^6$/ft plots.



Smooth model | ASTM-230 | ASTM-140 | ASTM-80

ASTM-40 | ASTM-20 | ASTM-10

Figure 22. Roughness height effects, sphere-cone geometry, $Re_\infty = 5.0\times10^6$/ft images.

C. Boundary Layer Transition Correlation

Boundary-layer transition onset locations were determined for all streamlines at each test condition through examination of the Reynolds number effects line plots of heating vs. streamline distance. Following the procedure detailed in Ref. [1], transition onset locations were identified through the tangent-slope-intercept method. This method provides a consistent "apparent" transition location that can be clearly determined through analysis of surface temperature or heat transfer data. However, this location is probably slightly downstream of the point in the boundary-layer at which the small disturbances that produce transition actually begin.

In all, this test program provided 3024 potential measurements (36 streamlines *x* 6 Reynolds numbers *x* 7 roughness heights patterns *x* 2 geometries) of transition location over relevant three-dimensional entry vehicle geometries. After discounting the data from streamlines ϕ = 160 – 200 deg. due to the viewing angle difficulty, and also discounting those low Reynolds number / small roughness height cases where the flow remained laminar and the high Reynolds number / large roughness height where the flow was turbulent at the stagnation point, 1892 actual data points were generated. These transition onset data points are tabulated in Ref. [1].

In Refs. [2-3], a database of 451 transition onset locations on hemispherical nosetip geometries from flight, wind tunnel, and ballistics range tests was assembled and analyzed in order to correlate the effects of distributed, sand-grain type roughness on boundary-layer transition. The resulting correlation was given by the Eqs. (1) –(3).

$$Y_{TR} = 165 \times (X_{TR})^{-0.5} \tag{1}$$

where the flow field parameter Y_{TR} is:

$$Y_{TR} = (Re_\theta)_{TR} \tag{2}$$

and the disturbance parameter X_{TR} is:

$$X_{TR} = \left[\left(\frac{k}{\theta}\frac{T_e}{T_w}\right)\left(\frac{H_e}{H_k}\right)^{-1}(M_e)^{-0.5}\right]_{TR} \tag{3}$$

In this correlation, the roughness height parameter *k* was taken to be the 50% peak-to-valley exceedance value k_{PV50}, as defined previously. As discussed in Refs. [2-3], this formulation was effective in correlating the data set. However, when this correlation was applied to the hexcomb pattern roughness data obtained on the spherical-cap and spherical cone geometries, it was evident that the effects of a variable surface pressure gradient over the surface needed to be included in the correlation. Accordingly, the pressure gradient effects were incorporate through an additional term derived from the Pohlhausen parameter:

$$\beta_{POHL} = \left\{10^{[min(10,max(-10,\lambda_{POHL}))]/10}\right\}^{-1} \tag{4}$$

where the Pohlhausen parameter is defined as:

$$\lambda_{POHL} = \frac{dU_e}{ds}\frac{\delta^2}{\nu_e} \tag{5}$$

The complicated definition for this modified Pohlhausen parameter, β_{POHL}, is required to ensure that the value remains bounded and positive. Because the original Pohlhausen parameter is a pressure-gradient term that can be

positive or negative over the surface, this definition provides a positive value required for exponentiation, while the min/max limits ensure that the value does not cause computational under/over flow.

The exponents on the modified Pohlhausen parameter and the original components of the disturbance terms were parametrically varied to find a new best fit definition as:

$$X_{TR} = \left[\left(\frac{k}{\theta} \frac{T_e}{T_w} \right)^{0.45} \left(\frac{H_e}{H_k} \right)^{-1.8} (M_e)^{-0.6} (\beta_{POHL})^{-0.5} \right]_{TR} \quad \textbf{(6)}$$

where:

$$k = \begin{cases} k_{PV50} & \text{sand-grain distributed} \\ h & \text{hexcomb pattern} \end{cases} \quad \textbf{(7)}$$

The new correlation equation for roughness-induced boundary layer transition, which includes pressure gradient effects and accounts for both distributed sand-grain and hexcomb pattern roughness is then given by:

$$Y_{TR} = 171.4 \times (X_{TR})^{-0.6299} \quad \textbf{(8)}$$

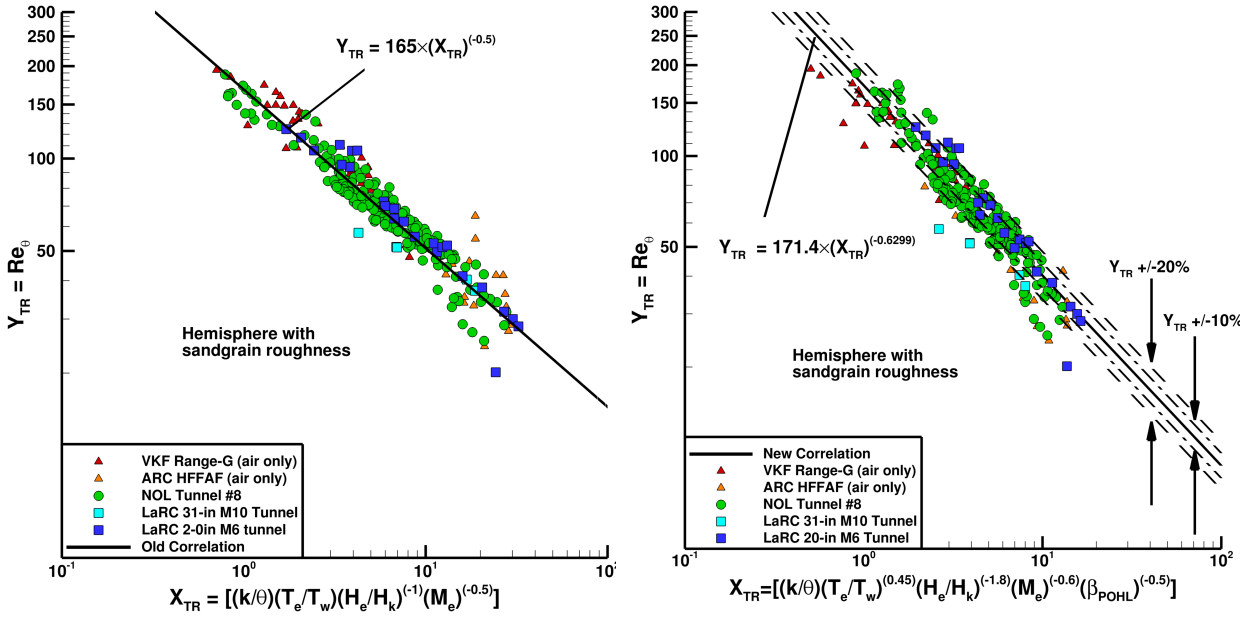
Comparisons of the effectiveness of the original and modified transition correlations for the prior data sets are shown in Figure 23 for the hemispherical geometry with sand-grain distributed roughness, Figure 24 for the spherical-cap geometry with hexcomb pattern roughness and Figure 25 for the sphere-cone geometry with hexcomb pattern roughness.

Comparisons of the modified correlation with the current sand-grain distributed roughness data on the three-dimensional sphere-cone and spherical-cap geometries are given in Figure 26. While this new distributed sand-grain roughness data set follows the same trend line as the correlation, it exhibits considerably more scatter than earlier data sets, with some transition points falling outside the ±50% uncertainty bounds. However, there is a key characteristic of the current data set that differs from prior data sets, which is the variability of roughness height over the surface of a wind tunnel model.

As discussed earlier, the roughness elements in the current data set were found to exhibit an approximately Gaussian height distribution due to the method in which the roughness elements were created. The height values used in this analysis represent the 50% exceedance value, which means that half of the roughness elements have a larger height than the specified value and half have a smaller height. In contrast, the roughness heights for the prior studies were much more uniform either in practice or in effect. For the earlier hexcomb pattern roughness study, the hexcomb sizes were defined uniformly in the CAD design of the models and were fabricated as such. For the earlier distributed sand-grain roughness hemisphere models, the same fabrication process used in this study was also used to create the sand-grain roughness patterns, resulting in a Gaussian distribution of heights. However, because of the axisymmetric nature of a hemispherical flow field, the transition data were reported as an average of *all* streamlines around the circumference of the model, which effectively provided a uniform average height and greatly reduced the scatter in the data set.

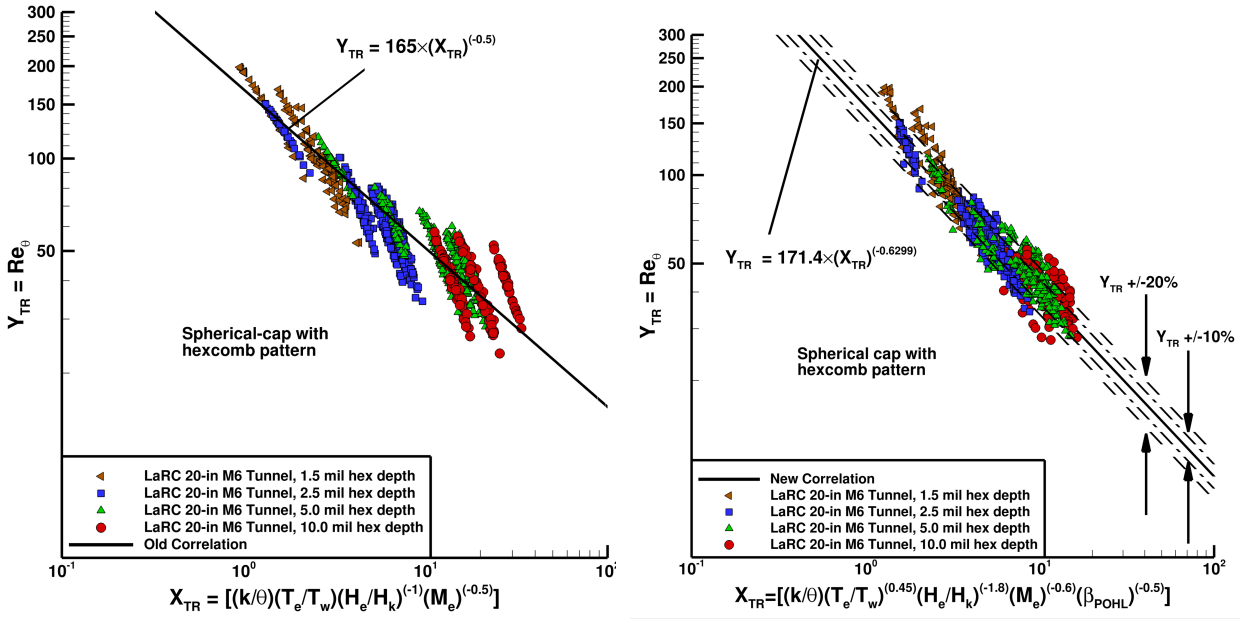
Given these differences in the definition and reporting of the roughness heights between these studies, it is not surprising that the current data exhibit much more scatter than the earlier data. The current distributed sand-grain roughness data set is in fact, probably a more "flight-realistic" representation of roughness transition characteristics. The TPS of an actual flight vehicle is likely to exhibit more variability in roughness due to manufacturing defects, damage during handling and flight preparation, and random variations in material response. A real-world example of nonuniform transition response is illustrated in Figure 27 by a post-flight photograph (from Ref. [16]) of the Orion EFT-1 flight test mission heat shield. While the green-outlined areas that identify damage during recovery of the heatshield can be disregarded, the red-outlined areas represent isolated transition wedges caused by nonuniformities in the surface ablation of the heatshield.

Since the new transition data follow the same trend as the earlier data, albeit with much more scatter, no modifications will be made to the transition correlation defined by Eqs. (4) –(8). However, these wind tunnel data – and the flight data from EFT-1 – illustrate the need to consider large margins on the transition predictions to account for potential variations in roughness heights from an expected nominal value.



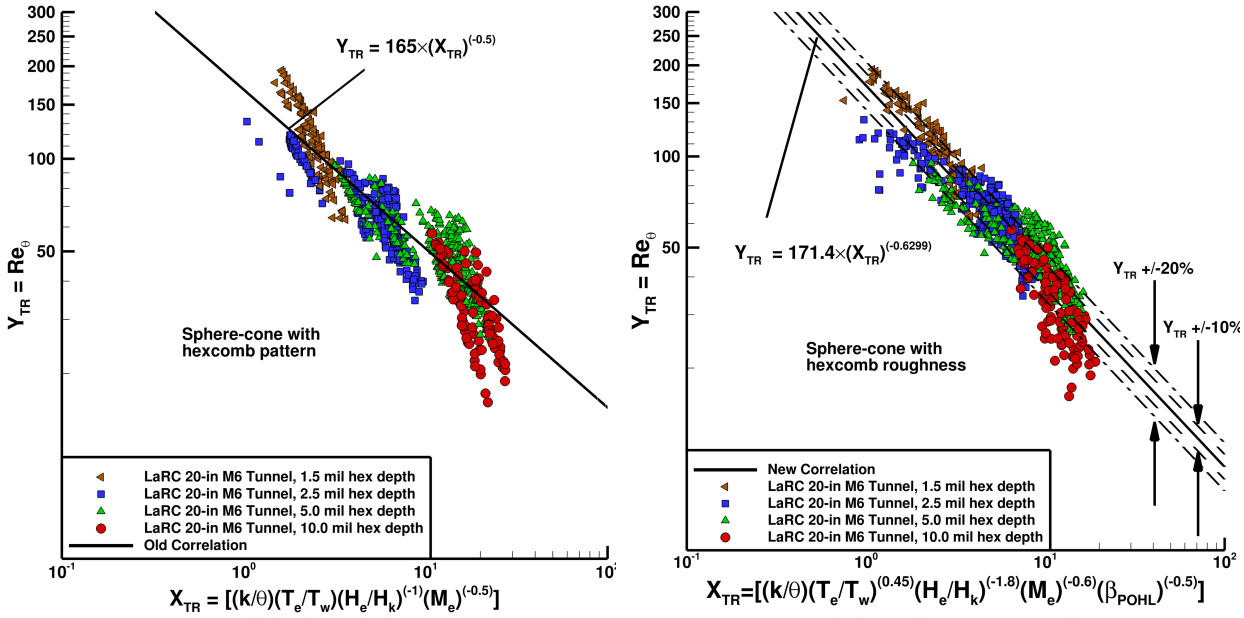
a) Original correlation b) New correlation with pressure gradient term

Figure 23. Roughness correlations applied to hemisphere geometry with distributed sand-grain roughness.



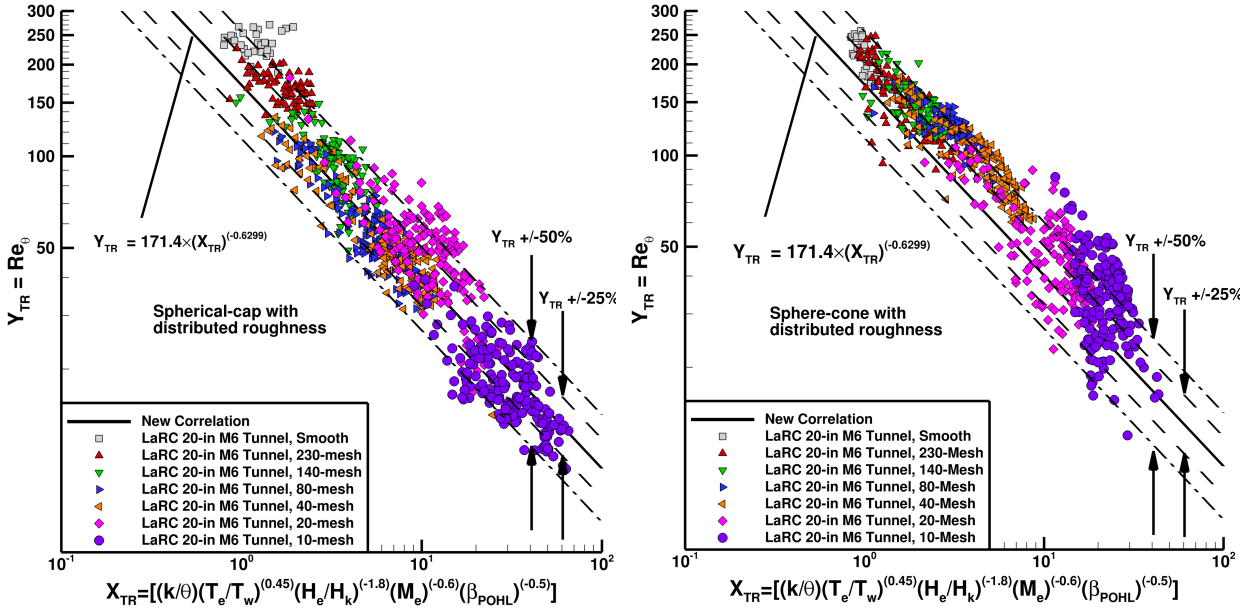
a) Original correlation b) New correlation with pressure gradient term

Figure 24. Roughness correlations applied to spherical-cap geometry with hexcomb pattern roughness.



A) Original correlation B) New correlation with pressure gradient term

Figure 25. Roughness correlations applied to sphere-cone geometry with hexcomb pattern roughness.



A) Spherical-cap geometry B) Sphere-cone geometry

Figure 26. Roughness correlations applied to spherical-cap and sphere-cone geometries with distributed sand-grain roughness.

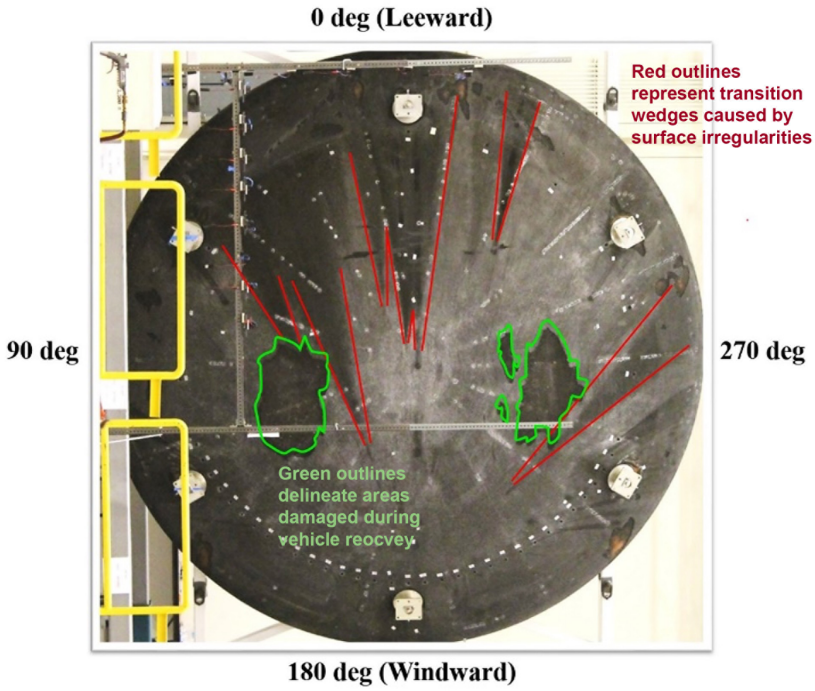


Figure 27. Post-flight recovery picture of Orion EFT-1 heatshield [source NASA]

V. Summary and Conclusions

The effects of distributed sand-grain surface roughness on boundary-layer transition and turbulent heating have been investigated through hypersonic wind tunnel testing of two representative entry vehicle geometries with roughness patterns simulating those of a heat shield with an ablated TPS. Convective heating data were obtained at Mach 6 over a range of roughness heights and free stream Reynolds numbers sufficient to produce laminar, transitional and turbulent flow. Boundary-layer transition onset locations were extracted along multiple surface streamlines for each model.

Laminar and turbulent smooth surface computational flow field simulations were performed for all test conditions for comparison with the heating data and to provide boundary-layer parameters for correlation of the transition data. The smooth surface laminar heating data and predictions were in good agreement for all conditions. The measured turbulent heating augmentation above smooth-wall predictions grew larger with increasing roughness height.

A boundary-layer transition correlation developed from pattern hexcomb roughness data sets was evaluated for applicability to the current data set. Although the distributed sand-grain roughness exhibited more scatter than previous data sets, the correlation was deemed to be suitable.

VI. Acknowledgements

This work was supported by the NASA Entry Systems Modeling Project within the Game Changing Development Program of the Space Technology Mission Directorate.

VII. References

1. Hollis, B. R. and Hollingsworth, K. E., "Experimental Investigation of Distributed Sand-Grain Roughness Effects on Transition Onset and Turbulent Heating Augmentation at Mach 6," NASA-TM-2022-5643, April 2022.
2. Hollis, B. R., "Correlation of Recent and Historical Hemispherical Nose Tip Distributed Roughness Transition Data," *Journal of Spacecraft and Rockets*, Vol. 56, No. 5, May-June 2019, pp. 664-686.
3. Hollis, B. R., "Experimental Investigation of Roughness Effects on Transition Onset and Turbulent Heating Augmentation at Mach 6 and Mach 10," NASA/TM-2017-219613, May 2017.
4. Hollis, B. R., "Hexcomb-Pattern Roughness Effects on Blunt-Body Transition and Heating," *Journal of Spacecraft and Rockets*, Vol. 58, No. 6, November-December 2021, pp. 1612-1635.

5. Hollis, B. R., "Experimental Investigation of Hexcomb-Pattern Roughness Effects on Transition Onset and Turbulent Heating Augmentation at Mach 6," NASA/TM-2019-220424, November 2019.
6. ASTM E11-01, Standard Specification for Wire Cloth and Sieves for Testing Purposes, ASTM International, West Conshohocken, PA, 2001.
7. Dirling, R. B., "On the Relationship Between Material Variability and Surface Roughness," AIAA Paper 1977-0402, 18th Structural Dynamics and Materials Conference, San Diego, CA, March 21-23, 1977.
8. Berger, K., Rufer, S., Hollingsworth, K. and Wright, S., "NASA Langley Aerothermodynamic Laboratory: Hypersonic Testing Capabilities," AIAA Paper 2015-1337, 53rd AIAA Aerospace Sciences Meeting, Kissimmee, FL, January 5-9, 2015.
9. Hollis, B. R., Berger, K. T., Berry, S. A., Brauckmann, G. J., et al, "Entry, Descent, and Landing Aerothermodynamics: NASA Langley Experimental Capabilities and Contributions," AIAA Paper 2014-1154, AIAA 52nd Aerospace Science Meeting, National Harbor, MD, January 13-17, 2014.
10. Fay, J. A., and Riddell, F. R., "Theory of Stagnation Point Heat Transfer in Dissociated Air," *Journal of Aeronautical Sciences*, Vol. 25, No. 2., February 1958, pp. 73-85.
11. Buck, G. M., "Surface Temperature/Heat Transfer Measurement Using a Quantitative Phosphor Thermography System," AIAA Paper 91-0064, 29th Aerospace Sciences Meeting, Reno, NV, January 7-10, 1991.
12. Merski, N. R., "Global Aeroheating Wind-Tunnel Measurements Using Improved Two-Color Phosphor Thermography Methods," *Journal of Spacecraft and Rockets*, Vol. 36, No. 2, March-April 1999, pp. 160-170.
13. Mason, M. L. and Rufer, S. J., "Imaging for Hypersonic Experimental Aeroheating Testing (IHEAT) version 4.0: User Manual," NASA/TM-2018-220113, November 2018.
14. Gnoffo, P. A., "An Upwind-Biased, Point-Implicit Algorithm for Viscous, Compressible Perfect-Gas Flows," NASA TP-2953, February 1990.
15. Thompson, K. B., Hollis, B. R., Johnston, C. O., Kleb, B., Lessard, V. R, and Mazaheri, A., "LAURA User's Manual: 5.6," NASA TM-2020-220566, February 2020.
16. Vander Kam, J. and Amar, A. "Orion Aerosciences and Thermal Protection System Overview," NASA Engineering and Safety Center, EDL Summer Series lecture, July 2021.